Composite Structures 341 (2024) 118129

Contents lists available at ScienceDirect

Composite Structures

journal homepage: www.elsevier.com/locate/compstruct

Fatigue and post-fatigue behavior of FRCM-concrete specimens under direct shear and bending conditions

Angelo Savio Calabrese, Pierluigi Colombi, Tommaso D'Antino *

Department of Architecture, Built Environment and Construction Engineering, Politecnico di Milano, Milan, Italy

ARTICLE INFO

Keywords:
FRCM
Fatigue
Bond
Direct shear test
RC beam

ABSTRACT

The combined effect of cyclic loading and steel rebar corrosion can determine the premature deterioration of reinforced concrete (RC) structures subjected to dynamic and environmental actions. The use of fabric-reinforced cementitious matrix composites (FRCM) is a promising solution to extend the fatigue life of RC structures. Externally bonded FRCMs are applied to the tension side of structural members to reduce the rebar stress level, thus delaying fatigue crack nucleation and/or propagation. A key aspect for the design of FRCM strengthening of these structures is the matrix-fiber bond behavior under fatigue loading. In this paper, a critical review of currently available studies on the fatigue behavior of FRCM-strengthened RC beams is presented. Then, the results of 25 bond tests on PBO FRCM-concrete specimens are provided and discussed. These tests include both single-lap direct shear and modified beam tests performed in quasi-static and cyclic mode. The results obtained show that the cyclic load may induce progressive debonding at the matrix-fiber interface with rupture of fiber filaments. Modified beam tests are more affected by these phenomena than direct shear tests. The rupture of fiber filaments is confirmed by the results of post-fatigue tests that show capacities lower than those of corresponding quasi-static tests.

1. Introduction

The remarkable increase of traffic volume and vehicles weight in recent years has been enhancing the fatigue loading of reinforced concrete (RC) viaducts and bridges [1,2]. Among possible issues, cyclic loading may induce the formation and propagation of fatigue cracks in steel rebar, which may eventually result in fatigue failure. Besides, the corrosion of steel rebar can determine a further increase in the fatigue vulnerability [3].

Current design guidelines require stresses in RC members during the structure service life to be lower than the endurance limit of the specific material, i.e., the threshold stress level below which fatigue failure is prevented (safe life approach fatigue design [4]). Accordingly, ACI 215R-92 [5] defines the tensile fatigue strength of plain concrete and steel rebar as 55 % and 45 %-60 % of the corresponding quasi-static tensile and yield strength, respectively. Similarly, Eurocode 2 [6] allows the use only of steel rebars that did not show any fatigue damage when subjected to at least 2 million cycles at a stress range larger than 150 MPa and a maximum stress within 60 % of the bar yielding strength.

Nowadays, many existing bridges and viaduct close to their service life require strengthening or retrofitting to increase their fatigue life due to increase of applied loads, poor construction quality and/or maintenance level, and deterioration induced by environmental actions. As an alternative to traditional strengthening/retrofitting solutions [7], fiber-reinforced polymers (FRP) externally bonded (EB) to the tension side of RC structural elements were proven to be effective in improving the member fatigue life without significant increment of the dead weight and with no traffic disruption [8,9]. EB FRP applications proved to be effective for the fatigue strengthening of metallic and reinforced concrete structures [10,11]. However, cyclic actions may induce FRP-substrate interface debonding, leading to a premature and brittle failure of the strengthened member [8].

As an alternative to the use of FRP composites, EB inorganic-matrix composites comprising high-strength fiber textiles embedded within an inorganic matrix have been proposed for the strengthening of RC and masonry members. These composites are usually referred to as textile reinforced mortar (TRM), fabric-reinforced cementitious matrix (FRCM, nomenclature adopted in this paper), or steel reinforced grout (SRG, when steel fiber is employed for the textile reinforcement) [12]. The use of an inorganic matrix rather than the organic resin adopted in FRP

* Corresponding author.
E-mail address: tommaso.dantino@polimi.it (T. D'Antino).

https://doi.org/10.1016/j.compstruct.2024.118129
Received 1 December 2023; Received in revised form 23 February 2024; Accepted 12 April 2024
Available online 14 April 2024

composites allows for having a better compatibility with concrete and masonry substrates, higher durability with respect to different environmental exposure, and higher resistance to relatively high temperature [13]. However, due to the peculiarity of each FRCM, further studies are needed to clearly identify the long-term behavior of these composites. Results previously obtained by the authors indicate a limited detrimental effect of humidity, saline and alkaline environments, wet-dry cycles, freeze–thaw cycles, and high temperatures (i.e., 100° C) on the tensile mechanical and bond properties of FRCM [14,15].

Experimental, analytical, and numerical studies showed that EB FRCM composites are effective in increasing the flexural, shear, and axial capacity of RC beams and columns [16,17], as well as the in- and out-of-plane capacity of structural and non-structural masonry elements [18,19]. However, the contribution of FRCM to the member capacity is often limited by the occurrence of debonding failures. Accordingly, in the last decade numerous efforts were made to deeply understand the FRCM-substrate quasi-static bond behavior employing direct shear (DS) and modified beam (MB) bond test set-ups [20–22]. Nevertheless, very limited information is available on the effect of cyclic loading on the FRCM tensile and bond behavior [23,24]. In DS tests, the matrix-fiber interface is mainly subjected to shear stress, which allows for assuming a pure fracture mechanics Mode-II loading condition at this interface. In indirect shear test set-ups, such as notched beam (NB) and MB set-ups, the matrix-fiber interface is subjected to both shear and normal stresses, which affect the bond behavior [20,25]. Due to their specific features, the DS set-up is used to study the matrix-fiber bond behavior (mainly) under a Mode-II loading condition, whereas the MB set-up provides information on the interface behavior of composites subjected to a mixed Mode-I/II loading condition [26,27]. The presence of stresses normal to the matrix-fiber interface was proved to increase the quasi-static capacity associated with MB tests with respect to that of corresponding DS tests. However, these stresses can induce failure of fiber filaments, thus decreasing the residual capacity of the interface [20].

In this paper, an in-depth review of the currently available studies on the fatigue behavior of FRCM strengthened RC beams is first presented to clarify the role of the composite in the beam load-carrying capacity, its exploitation rate under service and ultimate loads, and how the steel reinforcement ratio, load range, and load frequency affect the strengthened beam fatigue behavior. Then, the results of an experimental campaign including both DS (9 specimens) and MB (16 specimens) fatigue bond tests on polyparaphenylene benzobisoxazole (PBO) FRCM-concrete specimens are presented and discussed. Results of MB tests, in which the specimen deflection induces stresses normal to the composite plane, are compared with those of corresponding DS tests where a pure Mode-II loading condition is assumed. The results obtained shed light on the effect of beam deflection on the composite behavior under fatigue loading.

2. Fatigue strengthening of RC beams with FRCM composites: State of the art

The load–deflection response of FRCM-strengthened or retrofitted RC beams subjected to a cyclic bending action can be divided in three main phases [28–31]. The first phase is characterized by a rapid decrease of the beam flexural stiffness caused by the opening of flexural cracks in concrete and FRCM matrix. A second phase follows, which characterizes most of the specimen fatigue life. In this phase, flexural cracks propagate toward the compressive zone of the beam and stresses acting on tension rebars and FRCM composite progressively increases with the reduction of the neutral axis depth. This in turn determines the initiation of a fatigue crack in the steel rebars that propagates steadily throughout the second phase determining a gradual increase of the beam deflection and local debonding of the FRCM composite [30]. Eventually, in the third phase the rate of rebar fatigue crack propagation rapidly increases until the resisting cross-section is no longer able to withstand the stress induced by the cyclic load. A sudden failure of the bar occurs, which results in large deflection of the beam, FRCM debonding, and eventual element collapse.

The presence of the FRCM strengthening affects the beam fatigue behavior. In [28], it was pointed out that the degradation rate observed in the beam second phase (i.e., the steady phase) was lower in strengthened than in corresponding control (non-strengthened) RC beams, due to the crack bridging effect provided by the FRCM textile. Su et al. [31] observed that the presence of the FRCM composite determined the formation of thinner and more spaced flexural cracks in comparison with those of control beams. The presence of multiple fine cracks can improve the RC beam fatigue performance [32] and reduce the rebar exposure to the external environment, thus limiting its corrosion [29,31,33]. In [34], it was shown that the effectiveness of the FRCM in increasing the fatigue life of RC beams was affected by the composite reinforcement ratio, which expresses the potential FRCM strength contribution with respect to the tension steel strength contribution [30,33]. Accordingly, moderately strengthened beams showed higher fatigue life enhancements with respect to poorly strengthened beams. However, this effect was not observed in highly strengthened beams, which did not show significant increase of fatigue life with respect to moderately strengthened ones. This result could be attributed to the occurrence of different failure modes in beams strengthened with 3 and 5 textile layers, as observed also in multilayer FRCM-concrete joint direct shear tests [35]. The study also showed that, independently from the type of fiber employed, an almost linear relationship between the maximum applied fatigue load and the specimen fatigue life could be identified. However, when the fatigue load induced a stress in tension rebars lower than their endurance limit, all specimens reached the target number of cycles without failure.

To investigate the contribution provided by the FRCM composite in the strengthened beam fatigue life and to determine the composite exploitation during the cyclic load, the experimental results presented in six relevant studies available in the literature were considered [28,30,31,33,36,37]. Other similar studies were not considered due to the unavailability of fundamental data. The studies considered included beams with corroded steel reinforcement, which in some cases entailed for the occurrence of rebar yielding [31]. Although FRCM composites effectively increase the beam bending strength, their contribution under service load may be low due to their limited cross-sectional area and to the fact that a relevant part of the service load (mainly dead loads) is already acting on the RC beam when the strengthening is applied.

The geometry of specimens considered is reported in Table 1 with reference to the parameters depicted in Fig. 1. The reinforcement ratio ρ_t defined in Eq. (3) is reported in Table 1 for each beam. The main test parameters, such as the fatigue maximum ($P_{\max}$) and minimum ($P_{\min}$) loads, the frequency f, the FRCM textile cross-sectional area A_f, the cracked elastic modulus E_f (as defined by ACI 549.6R-20 [12]), and the fatigue life N_F are reported in Table 2 for each specimen. Finally, in Table 2 $\varepsilon_{f,\max}$ is the FRCM strain at the fatigue cycle peak while the rebar stress reduction rate ξ and the exploitation ratio η are defined in Eq. (2) and Eq. (4), respectively.

FRCM strengthening can be adopted to reduce the stress acting in the steel reinforcement or to increase the load that can be applied to the member under service conditions. In both cases, the FRCM contribution to the member capacity is affected by the composite axial stiffness and by the capacity associated with the composite-concrete stress-transfer mechanism [28], which mainly depends on the matrix-fiber impregnation capability and on the matrix compatibility with the substrate [29,40]. Assuming perfect bond at the steel concrete and composite-concrete interfaces, the contribution of FRCM to the beam flexural capacity can be evaluated by enforcing the cross-section equilibrium at the beam midspan (see Fig. 1):

Table 1
Main geometrical characteristics of strengthened beams considered.

Reference	Set-up		RC beam							FRCM	
	l_b (mm)	l_k (mm)	L (mm)	b (mm)	h (mm)	d (mm)	A_c (mm^2)	A_t (mm^2)	ρ_t (%)	l_f (mm)	b_1 (mm)
Aljazaeri and Myers 2017 [37]	2032	254	2133	203	305	268	157	236	0.43	1880	203
Elghazy et al. 2018 [28]	2560	800	2800	150	250	225	101	402	1.19	2400	150
Pino et al. 2017 [30]	1524	0	1829	152	305	268	142	213	0.52	1524	152
Akbari Hadad et al. 2018 [36]	1524	0	1829	152	305	268	142	213	0.52	1524	152
Akbari Hadad and Nanni 2020 [33]	1524	0	1829	152	305	268	142	213	0.52	1524	152
Su et al. 2020 [31]	1200	400	1500	170	300	262	100	226	0.51	1100	170

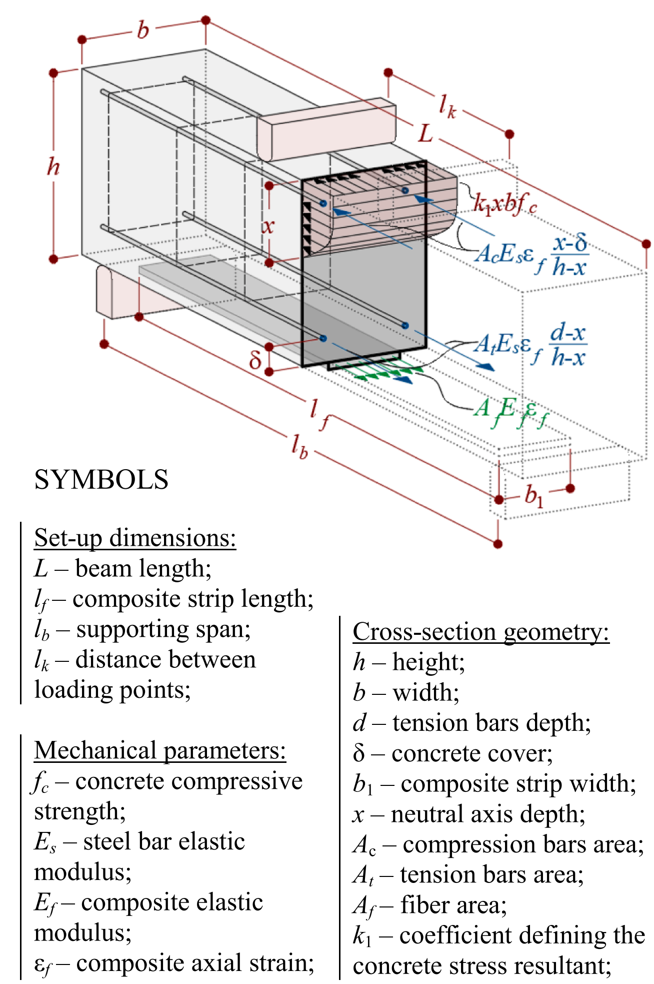

Fig. 1. Test set-up and cross-section forces under pure bending condition.

$$\begin{cases} k_1xbf_c+A_c\min\left\{E_s\varepsilon_f\left(\dfrac{x-\delta}{h-x}\right),f_{yc}\right\}-A_t\min\left\{E_s\varepsilon_f\left(\dfrac{d-x}{h-x}\right),f_{yt}\right\}-A_fE_f\varepsilon_f=0 \\ k_1xbf_c(d-k_2x)+A_c\min\left\{E_s\varepsilon_f\left(\dfrac{x-\delta}{h-x}\right),f_{yc}\right\}(d-\delta)+A_fE_f\varepsilon_f(h-d)=M \end{cases} \quad (1)$$

where k_1 and k_2 are coefficients that define the concrete compressive force value and position, respectively [41], f_c is the concrete compressive strength, ε_f is the FRCM strain, E_s is the elastic modulus of tension steel, assumed equal to 200 GPa, f_{yc} and f_{yt} are the compression and tension steel bar yielding stresses, respectively, E_f is the FRCM cracked elastic modulus according to AC434 and ACI 549.6R-20 [12,42] (see Table 2), respectively, x is the neutral axis depth, and M is the acting bending moment. It is worth noting that the Italian guideline for FRCM design [43] considers the bare textile elastic modulus rather than the cracked elastic modulus E_f. In Eq. (1), which is based on the assumption that plane sections remain plane, a parabola-rectangle, elastic-perfectly-plastic, and linear-elastic response were assumed for concrete in compression, longitudinal steel, and FRCM composite, respectively [41]. It should be noted that in real applications the FRCM strengthening is usually applied when the dead load is already acting on the structure, which entails for the presence of stresses within the cross-section when the FRCM is applied. This aspect was disregarded in this study, since the only pre-existing load acting on the considered beams was the self-weight.

The FRCM contribution to the member capacity can be assessed by solving Eq. (1) considering the acting bending moment due to service loads $M = M_{serv}$. Assuming the same acting load before and after strengthening, the rebar stress reduction rate ξ is:

$$\xi = \frac{\sigma_{t,0}^{serv} - \sigma_{t,f}^{serv}}{\sigma_{t,0}^{serv}} \quad (2)$$

where $\sigma_{t,0}^{serv}$ and $\sigma_{t,f}^{serv}$ are the stresses in the steel tension reinforcement obtained from the solution of Eq. (1) with $M = M_{serv}$ and $A_f = 0$ (i.e., no FRCM strengthening) and $A_f \neq 0$, respectively. Considering specimens in Table 2 and M_{serv} defined as the bending moment that induced a tensile stress in the steel reinforcement equal to $\sigma_{t,0}^{serv} = 200$ MPa, ξ varied between 3.8 % and 13.7 % (see Table 2).

Fig. 2a shows the stress reduction rate ξ as a function of E_fA_f for representative specimens in Table 2. In this paper, E_fA_f was considered to account for the different mechanical properties and cross-sectional areas of FRCM studied. Fig. 2a shows that ξ increased with increasing E_fA_f with different trends depending on the steel reinforcement ratio ρ_t (Table 1):

$$\rho_t = \frac{A_t}{bd} \quad (3)$$

Accordingly, specimens in Fig. 2a could be grouped in two sets, one associated with 0.43 %$\leq\rho_t\leq$ 0.52 % and the other with $\rho_t = 1.19$ %. Considering each set individually (see Fig. 2a), the effectiveness of the FRCM in reducing the steel tensile stress appeared as a linear function of E_fA_f. For large values of ρ_t, the stress reduction rate provided by the FRCM remains (relatively) low even for large values of E_fA_f, since the cross-sectional area of tensile steel reinforcement is much higher than that of the FRCM. When ρ_t is low, the FRCM may provide stress reduction rates up to approximately 14 % (see Fig. 2a). However, it should be noted that in real applications these stress reductions may be lower than those computed in Fig. 2a due to the aforementioned possible presence of stresses in steel rebars, associated with the part of service load that is already acting on the structure when the FRCM is applied.

Eq. (1) was also solved enforcing $M = M_{max}$, being M_{max} the bending moment associated with the maximum fatigue load P_{max} applied experimentally, to evaluate the FRCM strain $\varepsilon_f = \varepsilon_{f,max}$ at the fatigue cycle peak. The values of $\varepsilon_{f,max}$ computed for specimens in Table 2 showed that, independently from the FRCM type employed and reinforcement ratio, the majority of the specimens with tensile rebars in the elastic range exhibited a strain approximately equal to 0.2 %, whereas only specimens with yielded tensile steel provided high values of $\varepsilon_{f,max}$.

Table 2
Main mechanical properties, parameters, and results of the experimental tests considered.

Reference	*Specimen*	*FRCM*	E_f [GPa]	A_f [mm^2]	P_{min}/P_u [%]	P_{max}/P_u [%]	f [Hz]	N_F [10^4]	$\varepsilon_{f,max}$ [-]	η [%]	ξ [%]
Aljazaeri and Myers 2017 [37]	B1-0	control	–	–	16	32	5	200	–	–	–
	B3-1	PBO	127	11.28	16	32	5	200	0.0015	n.d.	3.8
	B4-1	PBO	127	11.28	16	32	5	200	0.0015	n.d.	3.8
	B5-1	PBO	127	11.28	16	32	5	200	0.0015	n.d.	3.8
	B6-4	PBO	127	45.12	20	40	5	200	0.0024	16.5	13.7
	B7-4	PBO	127	45.12	20	40	5	200	0.0024	9.5	13.7
	B8-4	PBO	127	45.12	20	40	5	200	0.0024	9.7	13.7
Elghazy et al. 2018 [28]	FCU	control	–	–	21	60	2	39.6	–	–	–
	FCS-2P-I	PBO	121	15.00	21	60	2	54.5	0.0016	16.4	2.7
	FCS-4P-I	PBO	121	30.00	21	60	2	98.4	0.0018	13.3	5.3
	FCS-4P-II	PBO	121	30.00	21	60	2	149.3	0.0018	13.3	5.3
	FCS-3C-II	C	75	70.65	21	60	2	83.4	0.0022	12.4	7.6
Pino et al. 2017 [30]	F-CON-0-75a	control	–	–	13	48	2	91.9	–	–	–
	F-FRCM-3P-90	PBO	128	20.98	11	49	2	49.2	0.0024	8.5	7.6
	F-FRCM-3P-85	PBO	128	20.98	11	46	2	56.2	0.0022	8.0	7.6
	F-FRCM-3P-80a	PBO	128	20.98	11	44	2	200	0.0021	7.6	7.6
	F-FRCM-3P-80b	PBO	128	20.98	11	44	2	189	0.0020	7.1	7.6
	F-FRCM-3P-75a	PBO	128	20.98	11	41	2	200	0.0020	7.6	7.6
	F-FRCM-3P-75b	PBO	128	20.98	11	41	2	200	0.0021	7.1	7.6
	F-FRCM-1P-75	PBO	128	7.00	12	50	2	96.2	0.0020	n.d.	n.d.
	F-FRCM-5P-75	PBO	128	34.96	15	46	2	200	0.0020	–	–
Akbari Hadad et al. 2018 [36]	F-CON-75	control	–	–	14	51	2	82.4	–	–	–
	F-C200-75	C	65	13.38	13	49	2	133.4	0.0022	n.d.	n.d.
	F-C200-70	C	65	13.38	13	45	2	123.1	0.0020	n.d.	n.d.
	F-C200-65	C	65	13.38	13	42	2	200	0.0019	n.d.	n.d.
	F-C200-60	C	65	13.38	13	39	2	200	0.0017	n.d.	n.d.
	F-C600-75	C	64	47.73	11	41	2	152.6	0.0022	7.4	8.6
	F-C600-70	C	64	47.73	11	38	2	195.9	0.0021	6.9	8.6
	F-C600-65	C	64	47.73	11	35	2	200	0.0019	6.3	8.6
Akbari Hadad and Nanni 2020 [33]	F-CON-75	control	–	–	–	51	2	82.4	–	–	–
	F-ARG-85	G	20.3	95.46	–	65	2	31.6	0.0024	18.8	5.6
	F-ARG-75b	G	20.3	95.46	–	59	2	63.5	0.0021	16.9	5.6
	F-ARG-70	G	20.3	95.46	–	54	2	88.2	0.0019	15.4	5.6
	F-ARG-65	G	20.3	95.46	–	50	2	200	0.0018	14.3	5.6
	F-ARG-60	G	20.3	95.46	–	46	2	200	0.0017	13.3	5.6
Su et al. 2020 [31]	F0-I0-0.65	control	–	–	13	63	5	17.5	–	–	–
	F0-I20-0.65	control	–	–	13	63	5	20.6	–	–	–
	F2-I0-0.55	C	80[‡]	28.58	11	53	5	130	0.0023	10.7	6.3
	F2-I0-0.65	C	80[‡]	28.58	13	63	5	43.7	0.0027	12.8	6.3
	F2-I0-0.75	C	80[‡]	28.58	15	73	5	28.5	0.0048	22.6	6.3
	F2-I20-0.55	C	80[‡]	28.58	11	53	5	111.3	0.0023	10.7	6.3
	F2-I20-0.65	C	80[‡]	28.58	13	63	5	52.8	0.0027	12.8	6.3
	F2-I20-0.75	C	80[‡]	28.58	15	73	5	19.4	0.0052	24.7	6.3
	F2-I60-0.65	C	80[‡]	28.58	13	63	5	44.7	0.0027	12.8	6.3
	F2-I60-0.75	C	80[‡]	28.58	15	73	5	15.1	0.0048	22.6	6.3
	F2-I100-0.65	C	80[‡]	28.58	13	63	5	36	0.0027	12.8	6.3
	F2-I100-0.75	C	80[‡]	28.58	15	73	5	15.2	0.0048	22.6	6.3
	F2-I100-0.85	C	80[‡]	28.58	17	83	5	6.2	0.0104	49.7	6.3

Note: C = carbon, PBO = polyparaphenylene benzobisoxazole, G = alkali resistant glass, control = unstrengthened beam; [‡]Not declared in the original publication and assumed equal to that obtained for carbon and PBO FRCM in [38] and [39], respectively.

In Table 2, the FRCM exploitation ratio is defined as:

$$\eta = \frac{\varepsilon_{f,max}}{\varepsilon_{f,u}} \tag{4}$$

being $\varepsilon_{f,u}$ the FRCM strain at quasi-static beam failure. $\varepsilon_{f,u}$ was computed with Eq. (1) assuming $M = M_u$, where M_u is the bending moment associated with the experimental failure of nominally-equal FRCM-strengthened beams tested in quasi-static loading condition [28,30,31,33,36,37]. Fig. 2b shows the relationship between the FRCM exploitation ratio η and the fatigue life N_F of specimens analyzed. Specimens characterized by η>20 % [31], for which P_{max} was associated to yielding of tension rebars, exhibited the shortest fatigue life due to the high level of stress in the FRCM. For lower η values, an increase of N_F with decreasing η was observed for specimens within the same experimental campaign except for specimens in [37] that reached the runout limit set to 2 million cycles for any value of η considered. For some specimens (indicated with η= "n.d." in Table 2), the reference specimen quasi-static failure occurred due to concrete crushing, and the corresponding values of η were considered unreliable.

The analysis provided in this section highlights the potential contribution of FRCM externally bonded strips to the fatigue behavior of RC beams. The composite contribution is limited if the load acting on the beam when the composite is applied is similar to the service load acting on the strengthened beam. However, based on results in Fig. 2, even beams with low composite exploitation ratios showed failure before attaining 2 million cycles. This confirms the need for further research on the fatigue behavior of FRCM-strengthened RC members.

3. Experimental program

In the experimental campaign, 16 modified beam (MB) tests and 9 single-lap direct shear (DS) tests were performed to analyze the effect of cyclic load on the bond behavior of a PBO FRCM composite. The MB test allowed for studying the combined effect of cyclic normal and shear stresses (i.e., mixed Mode-II and negative Mode-I loading condition) on the composite bond behavior. Among the specimens considered, 6 MB

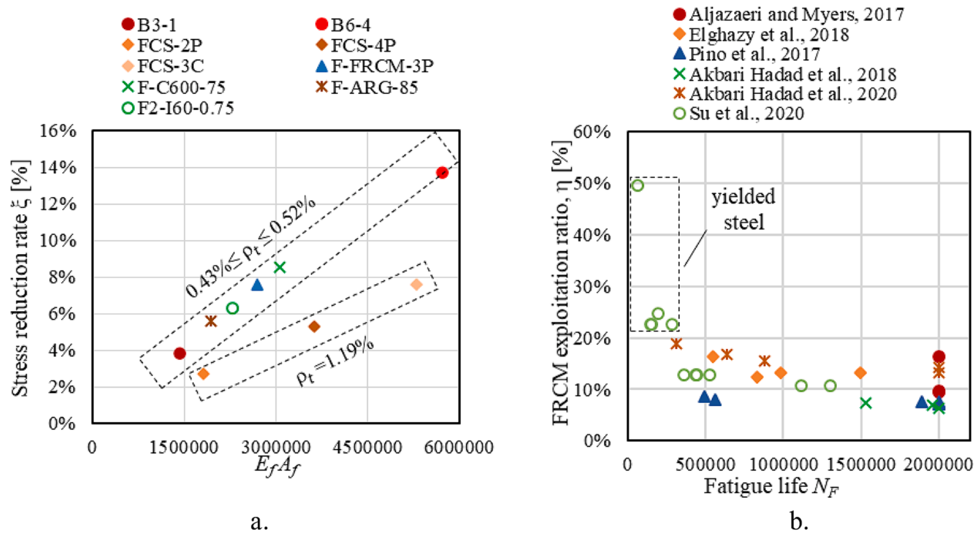

Fig. 2. State of the art analysis: a) steel stress reduction rate as a function of E_fA_f and b) FRCM exploitation ratio as a function of the fatigue life.

and 8 DS were subjected to quasi-static monotonic test. The remaining specimens were subjected to fatigue test with a fatigue load range calibrated on the results of corresponding quasi-static monotonic tests. For 2 MB specimens, the cyclic loading was interrupted and followed by quasi-static monotonic test up to failure to assess the degradation induced by the fatigue loading on the specimen capacity.

Specimens were named according to the notation MB(or DS)_X_Y_B (or G)_F(or PF)_n, where MB (=modified beam) or DS (=direct shear) indicates the test set-up, X is the bonded length (in mm), Y is the bonded width (in mm), B (=bare-fiber) or G (=bond-gap) indicates the strip layout in MB tests (see [20]), F or PF (if present) indicates a fatigue or post-fatigue test, respectively, and n is the specimen number.

It is worth noting that results of the quasi-static monotonic tests considered in this paper were previously presented in [20] and are reported here for completeness, while the preliminary results of specimens MB_300_60_B_F_1-4 were discussed in [34,44]. The results of these tests are considered in this work for comparison with corresponding results with a different layout (i.e., bond-gap) and test set-up (i.e., direct shear). Furthermore, the fatigue behavior of all specimens considered is analyzed in terms of global slip growth, cycle secant slope reduction, and increment of the area within the fatigue cycle (see Sections 3.3 and 4).

3.1. Specimen geometry and materials

Fig. 3 shows the geometry of DS and MB specimens considered in this study. Both test set-ups employed plain concrete prisms with nominal dimensions equal to 150 × 150 (cross-section) × 500 (length) mm. The concrete 28-day average compressive strength, tested according to EN 12390–3:2019 [45], was 37.9 MPa (CoV = 6.02 %) [44]. The FRCM

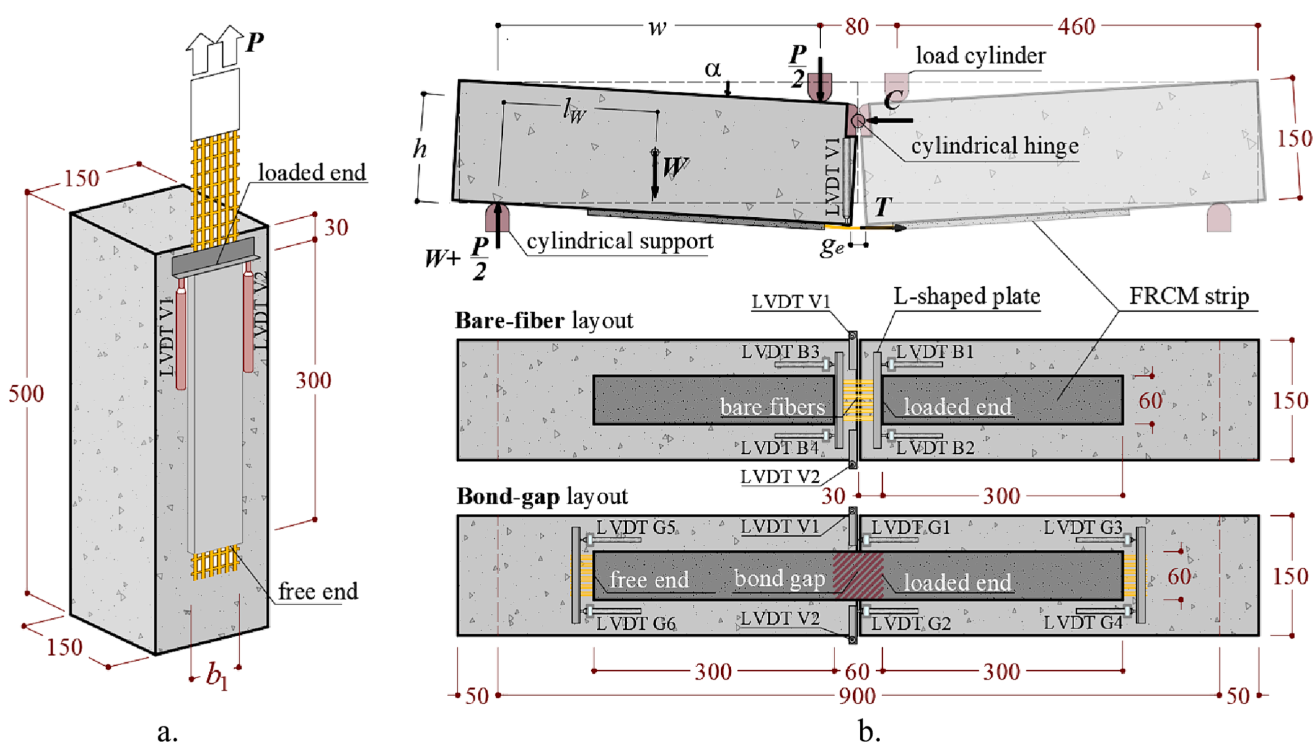

Fig. 3. Geometry of a) DS and b) MB specimens (dimensions in mm).

composite investigated in this paper was comprised of an open-mesh unbalanced PBO textile [46] embedded within a cement-based mortar [47]. The PBO textile had longitudinal yarns (i.e., aligned with the load direction) spaced at 10 mm on center and transversal yarns (i.e., orthogonal to the load direction) spaced at approximatively 17.5 mm on center. The composite width b_1 varied between 50 and 60 mm, depending on the number of yarns included in the textile layer (5 yarns for specimens DS_300_50_1-5 and 6 yarns for all other specimens). The FRCM bonded length was 300 mm for each prism, which resulted in a 600 mm overall bonded length for MB specimens. The cross-sectional area of each longitudinal bundle was 0.46 mm^2, resulting in an overall textile cross-sectional area $A_f = 2.76$ mm^2 when 6 yarns were considered (60 mm wide strip) or $A_f = 2.30$ mm^2 in the case of 5 yarns (50 mm wide strip).

The PBO textile mechanical properties were obtained with tensile tests of bare textile strips with different widths, according to EAD 340275–00-0104 [48]. The tensile strength and elastic modulus obtained were 3960 MPa (CoV = 6.96 %) and 241 GPa (CoV = 4.90 %), respectively [49]. The matrix compressive and flexural strength, tested according to UNI EN 1015–11 [50], were 51.60 MPa (CoV = 2.79 %) and 8.10 MPa (CoV = 16.30 %) [49], respectively, whereas the matrix tensile strength was estimated as 3.75 MPa using FRCM clevis-grip tensile tests [51].

In DS test, a composite strip was applied onto the concrete prism leaving a portion of textile bare at the loaded and free end (Fig. 3a). The concrete prism was restrained while the bare textile end, which was equipped with epoxy-bonded glass FRP tabs, was pulled.

In MB test, two prisms were connected by a cylindrical hinge located at the top (compression) side and an FRCM strip was bonded to the bottom (tension) side. A 4-point bending configuration was used, with two cylindrical supports spaced at 900 mm on center and load application points spaced at 80 mm (Fig. 3b). Two FRCM strengthening layouts were adopted, named bare-fiber (B) and bond-gap (G) (see [20]). In the former layout, a 60 mm long portion of textile was left bare (i.e., not embedded within matrix, see Fig. 3b) at the MB midspan, which allowed for a direct measurement of the relative slippage between fibers and matrix at the composite strip loaded ends (Fig. 3b). In the latter layout, the textile was embedded along the entire strip, whereas a 60 mm long FRCM portion at the MB midspan (named bond-gap) was not bonded to the substrate. The bond-gap layout was realized by applying a plastic tape to the concrete substrate along the 60 mm midspan portion before casting the FRCM strip.

In DS test, two linear variable displacement transformers (LVDTs) (V1 and V2 in Fig. 3a) were attached to the concrete block, on the two sides of the FRCM strip, and reacted off of an L-shaped aluminum plate bonded to the bare textile portion just outside the strip at the loaded end. The average of measurements of these LVDTs is named global slip g. In bare-fiber MB test, the global slip g was defined as the average of displacements measured by two LVDTs attached to the concrete on each side of the strip (named LVDT B1, B2, B3, and B4 in Fig. 3b) and reacting off of aluminum L-shaped plates bonded to the bare fibers immediately outside the matrix at the loaded ends. In bond-gap MB test, two LVDTs (LVDT G1 and G2 in Fig. 3b) were attached on the side of the FRCM strip to the same concrete prism at the MB midspan and reacted off of L-shaped aluminum plates bonded to the opposite prims. The average of measurements of these LVDTs is the relative displacement between blocks g_e (Fig. 3b). Other four LVDTs (LVDT G3, G4, G5, and G6, in Fig. 3b) were employed to measure the relative displacement between the textile and concrete at the strip free ends. Finally, in all MB tests, the vertical deflection at midspan was measured with LVDT V1 and V2 (Fig. 3b). Photos of specimens DS_300_60_F_1 and MB_300_60_B_F_3 before the beginning of the test are shown in Fig. 4 and Fig. 5, respectively.

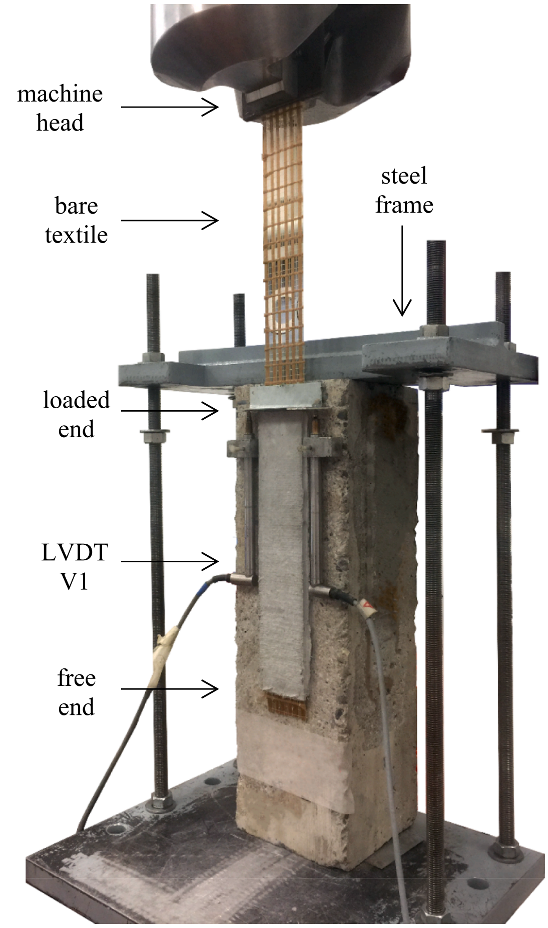

Fig. 4. Photo of specimen DS_300_60_F_1.

3.2. *Quasi-static monotonic tests*

Quasi-static monotonic tests were performed by monotonically increasing the displacement (stroke) of the machine head at a constant rate of 0.0034 mm/s. The composite axial stress at the loaded end $\sigma = P/A_f$ of DS tests was computed as the ratio between the load applied by the testing machine P and the textile cross-sectional area A_f. The fiber stress σ_0 acting at the loaded end of MB tests was computed according to Eq. (5) by enforcing the equilibrium to the free-body diagram in Fig. 3b:

$$\sigma_0 = \frac{T}{A_f} = \frac{Pw + 2Wl_W}{2h\cos\alpha}\cdot\frac{1}{A_f} \tag{5}$$

where α is the specimen rotation angle, w is the distance between one of the two loading points and the closest support, $W = 258$ N is the self-weight of the prism (assumed concentrated in its centroid), l_W is the horizontal distance between the prism centroid and the closest support, and h is the vertical distance between the axis of the cylindrical hinge and the textile plane (see Table 3).

Table 3 provides the main geometrical parameters, which are represented in Fig. 3a and b, of the quasi-static monotonic tests. Furthermore, the peak stress σ* (or σ_0* for MB tests), the corresponding global slip g* (or midspan displacement g_e* for bond-gap MB tests), the residual stress associated with the presence of friction at the matrix-fiber interface σ_f (or $\sigma_{0,f}$ for MB tests), and the corresponding global slip g_f (or $g_{e,f}$ for bond-gap MB tests) [20] are also represented in Fig. 6a and reported in Table 3 for each specimen.

All specimens failed due to debonding of the fiber from the embedding matrix. Fig. 6b, c, and d show the responses of quasi-static DS, bond-gap MB, and bare-fiber MB tests. MB tests provided a higher peak

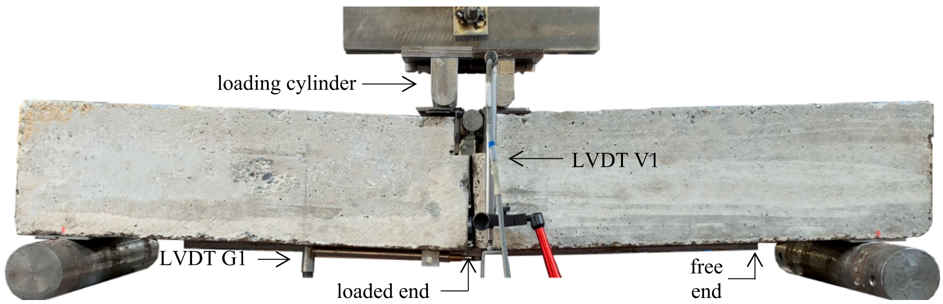

Fig. 5. Photo of specimen MB_300_60_G_F_3.

Table 3
Quasi-static monotonic experimental test results taken from [20].

Specimen	w [mm]	h [mm]	l_W [mm]	$L^{\dagger}$ [mm]	b_1 [mm]	σ^*, σ_0^* [MPa]	g^* [mm]	g_e^* [mm]	σ_f, $\sigma_{0,f}$ [MPa]	g_f [mm]	$g_{e,f}$ [mm]
DS_300_60_1					60	2090	0.95		123	5.98	
DS_300_60_2					60	1673	2.86		319	6.51	
DS_300_60_3					60	1813	2.15		112	6.20	
DS_300_50_1	–	–	–	300	50	1938	1.39	–	239	6.92	–
DS_300_50_2					50	2230	0.87		219	7.81	
DS_300_50_3					50	2224	1.22		231	7.03	
DS_300_50_4					50	2190	1.64		331	6.94	
DS_300_50_5					50	2148	1.15		269	6.92	
Average (•)	–	–	–	–	–	2038	1.53	–	230	6.79	–
CoV						0.102	0.441		0.350	0.083	
MB_300_60_B_1	410	150	200	300	60	2220	1.47		199	5.59	
MB_300_60_B_2						2124	2.47	–	481	5.51	–
MB_300_60_B_3						2135	1.61		430	5.85	
Average (•)	–	–	–	–	–	2159	1.83	–	370	5.65	–
CoV						0.024	0.243		0.406	0.026	
MB_300_60_G_1		150	200	300	60	2499		1.89	671		4.59
MB_300_60_G_2	410					2514	–	2.14	283	–	4.72
MB_300_60_G_3						2617		1.58	434		6.35
Average (•)	–	–	–	–	–	2543	–	1.87	463	–	5.22
CoV						0.025		0.149	0.422		0.188

† Bonded length of a single block; σ^*, σ_0^*=peak stress; g^*=global slip at peak stress; g_e^*=midspan displacement at peak stress; σ_f, $\sigma_{0,f}$ = residual stress; g_f = global slip at the first attainment of the residual (friction) stress; $g_{e,f}$ = midspan displacement at the first attainment of the residual (friction) stress.

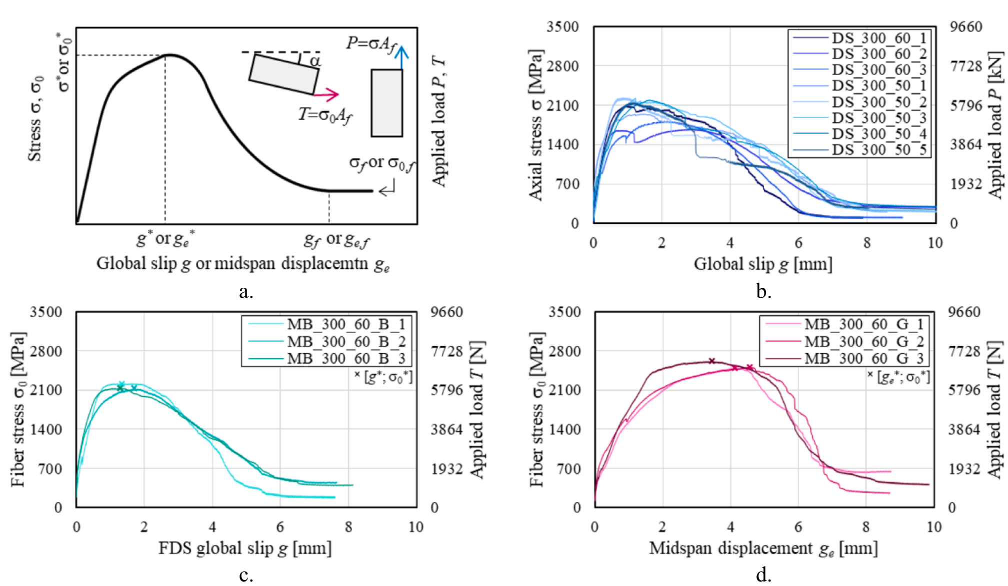

Fig. 6. Stress (or load) responses of DS and MB tests: a) idealized response; b) direct-shear tests; c) bare-fiber modified beam tests; d) bond-gap modified beam tests.

stress than DS tests (on average 24.8 % and 5.9 % higher for bond-gap and bare-fiber MB with respect to DS specimens, respectively), which was attributed to the presence of a normal stress component along the matrix-fiber interface in MB. This component, named σ_I in [20], was assumed localized at the composite loaded end and tended to push the fibers against the matrix internal layer (i.e., the layer in contact with the substrate) increasing the specimen load-carrying capacity. For this reason, the average residual (friction) stress of MB tests with bond-gap and bare-fiber layouts was 101.3 % and 60.9 % higher than that of DS tests, respectively. However, in some cases σ_I also induced damage to the fibers that eventually led to rupture of fiber filaments. This effect was more pronounced in bare-fiber than in bond-gap specimens, which was attributed to the sharp deviation of the textile axial direction in bare-fiber specimens due to the presence of the matrix discontinuity [20].

3.3. Fatigue tests

One DS and eight MB (four with bond-gap and four with bare-fiber layout) specimens were subjected to fatigue test. Photos of specimens DS_300_60_F_1 and MB_300_60_B_F_3 before the beginning of the test are shown in Fig. 4 and Fig. 5, respectively. Specimens were subjected to an initial quasi-static monotonic test in displacement (stroke) control at a constant rate of 0.0034 mm/s until the attainment of the mean cyclic load. Then, a force-controlled sinusoidal cyclic load with frequency 3 Hz [34,44] was applied to the specimen until failure was attained. The nominal minimum and maximum applied load in the fatigue cycles were equal to 25 % and 50 % of the average peak load of corresponding quasi-static monotonic tests, respectively, which were associated to a minimum and maximum stress σ_{min} = 510 MPa and σ_{max} = 1020 MPa for DS test, $\sigma_{0,min}$ = 550 MPa and $\sigma_{0,max}$ = 1050 MPa for bare-fiber MB test, and $\sigma_{0,min}$ = 635 MPa and $\sigma_{0,max}$ = 1270 MPa for bond-gap MB test. The actual average values of the applied fatigue stress measured during the test are provided in Table 4 for each specimen. These values were slightly different from the nominal values due to difficulties of the machine load-control mode in matching the command with the specimen response, which varied during the test. In Table 4, for MB and DS tests, respectively: T_{min} and T_{max} and P_{min} and P_{max} are the minimum and maximum applied fatigue loads (see Fig. 3a and b); $\overline{T}$ and $\overline{P}$ are the mean fatigue loads; $\Delta T = T_{max}$-T_{min} and $\Delta P = P_{max}$-P_{min} are the fatigue load ranges; $R_W = \sigma_{0,min}/\sigma_{0,max}$ and $\sigma_{min}/\sigma_{max}$ are the stress ratios; and N_F is the number of cycles to failure.

The axial stress σ – global slip g response of specimen DS_300_60_F_1 is presented in Fig. 7a. The first branch is associated with the quasi-static monotonic test up to the mean fatigue load, whereas blocks comprising 10 load cycles were selected during the fatigue test and are shown in Fig. 7a. The specimen response during the 10 cycles preceding failure is shown in a call-out in the same figure. The fatigue σ – g response of specimen DS_300_60_F_1, which resembled those observed in [24] on the same PBO FRCM composite tested with different fatigue load ranges, was characterized by three stages (see Fig. 7a): (i) an initial stabilization stage, (ii) an intermediate steady stage, and (iii) a non-steady final stage. The initial stage was limited to the initial (approximately) 500 cycles following the quasi-static monotonic branch. In this stage, the ratio between the current global slip g and the global slip at the end of the quasi-static monotonic branch, g_0, rapidly increased until attaining an approximately constant rate associated with the specimen steady stage (Fig. 7b). During this stage, which lasted for 85 % of N_F (i.e., up to approximately 18.2 × 10^5 cycles), the global slip steadily increased due to the progressive debonding and fiber damage. For the same reasons, the matrix-fiber interface stiffness decreased during this stage, as shown by the behavior of the cycle slope k (Fig. 7c), defined as the average slope of secant lines passing through the peaks and valleys of the cycles in a 10-cycle block (see Fig. 7a). This decrease of k was associated with an increase of the area enclosed by each cycle A_{cyc} (Fig. 7d), measured as the average area of the cycles in a 10-cycle block. With increasing the number of cycles, the specimen entered the non-steady stage (iii) where g rapidly increased until progressive failure of fiber filaments and eventual complete rupture of the textile occurred (see Fig. 7e). This failure was not localized in a unique cross-section. In fact, fiber filaments ruptured both inside and outside the bonded length. Since the fatigue test was load-controlled, no residual constant applied stress could be observed at the end of the test. In fact, due to progressive fiber filaments rupture, the specimens were no longer able to sustain the stress within the fatigue range applied, which determined the complete failure of the fibers.

4. MB Test fatigue and post-fatigue results

In this section, results of fatigue and post-fatigue MB tests are discussed. Fig. 8 illustrates the stress-global slip curve for both the bare-fiber and the bond-gap specimen fatigue tests. The σ_0-g responses of bare-fiber specimens (MB_300_60_B_F_1-4) are reported in Fig. 8a-d as they were previously presented in [34,44]. In specimens with bond-gap layout (MB_300_60_G_F_1-4), the presence of matrix along the bond-gap length (60 mm across midspan, see Fig. 3b) did not allow for a direct measurement of the global slip. Therefore, the average midspan displacement g_e measured by LVDTs G1 and G2 (see Fig. 3b) was considered for these specimens. Accordingly, Fig. 8e-h report the σ_0-g_e responses of specimens MB_300_60_G_F_1-4.

4.1. Bare-fiber specimens

The cyclic behavior of bare-fiber specimens was characterized by three stages (see Fig. 9a). During the initial stage, the FRCM strips on the two blocks behaved symmetrically and the global slips measured at the two loaded ends were almost identical for the same applied load. With increasing the number of cycles N, matrix-fiber debonding occurred on one side of the specimen, named fully debonded side (FDS), and the second stage began. At the FDS, g kept increasing with increasing N whereas it remained constant or slightly decreased at the opposite side, named partially debonded side (PDS). Eventually, during the last stage g progressively increased at a higher rate than in the previous stage and

Table 4
Fatigue test parameters and results.

Test	Specimen	T_{min} or P_{min} [kN]	T_{max} or P_{max} [kN]	$\overline{T}$ or $\overline{P}$ [kN]	ΔT or ΔP [kN]	$\sigma_{0,min}$ or σ_{min} [MPa]	$\sigma_{0,max}$ or σ_{max} [MPa]	R_W [-]	N_F [10^5]
MB	MB_300_60_B_F_1°	1.54	2.80	2.17	1.26	558	1015	0.55	2.03
	MB_300_60_B_F_2°	1.52	2.72	2.12	1.20	550	986	0.56	4.73
	MB_300_60_B_F_3°	1.50	2.96	2.23	1.47	542	1073	0.51	12.17
	MB_300_60_B_F_4°	1.48	2.94	2.21	1.46	537	1065	0.50	3.15
	Average	1.51	2.86	2.18	1.35	547	1035	0.53	5.52
	CoV	0.017	0.040	0.022	0.100	0.016	0.040	0.054	0.830
	MB_300_60_G_F_1	1.86	3.35	2.60	1.49	673	1212	0.56	0.42
	MB_300_60_G_F_2	1.85	3.40	2.62	1.55	669	1231	0.54	0.28
	MB_300_60_G_F_3	1.73	3.68	2.70	1.95	625	1332	0.47	0.32
	MB_300_60_G_F_4	1.74	3.71	2.72	1.97	629	1343	0.47	0.10
	Average	1.79	3.53	2.66	1.74	649	1279	0.51	0.28
	CoV	0.039	0.053	0.022	0.147	0.039	0.052	0.092	0.477
DS	DS_300_60_F_1	1.23	2.89	2.06	1.66	446	1046	0.43	21.15

° Presented in [34,44].

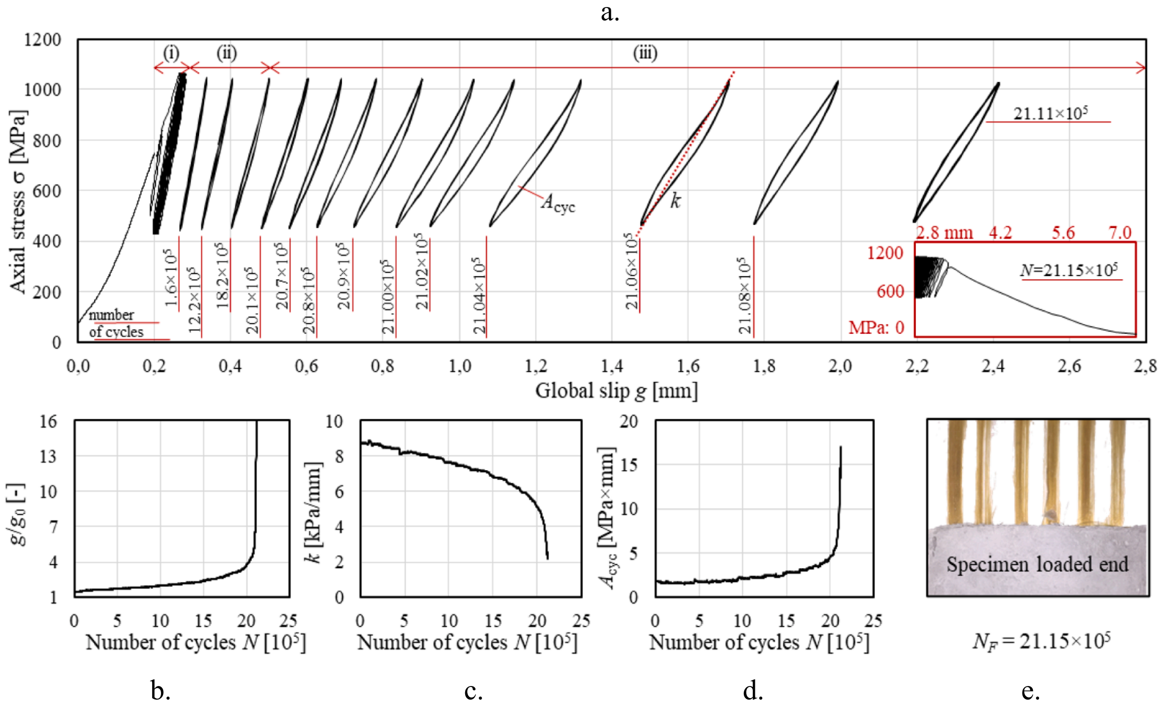

Fig. 7. Fatigue response of specimen DS_300_60_F_1: a) Axial stress σ − global slip g response and variation of b) normalized global slip, c) cycle secant slope, and d) cycle area with the number of cycles. e) Photo of the specimen loaded end at failure.

the specimen failed due to rupture of the textile strip at the specimen midspan. This indicated that the increase of g was not associated only to the propagation of debonding at the matrix-fiber interface but also to the subsequent rupture of fiber filaments [24,52]. The number of cycles at failure varied significantly (see Table 4). Specimen MB_300_60_B_F_1 failed after the lowest number of cycles, i.e., $N_F = 0.20 \times 10^6$. Specimens MB_300_60_B_F_2, 3, and 4 failed at $N_F = 0.47 \times 10^6$, 1.22×10^6, and 0.32×10^6, which are still limited compared to the 2.11×10^6 cycles attained in specimen DS_300_60_F_1.

To study the behavior of the global slip at the FDS, g was divided by the global slip at the beginning of the fatigue phase, g_0, since specimens provided different values of g at the end of the initial quasi-static monotonic branch. Analogously, the slope k was divided by the corresponding slope k_0 measured as the average of the slope of the first ten fatigue cycles. g/g_0, k/k_0, and A_{cyc} with respect to the number of cycles N are shown in Fig. 9a, b, and c for specimens MB_300_60_B_F_1-4. From Fig. 9a, it can be noticed that specimens that showed a rapid growth of g/g_0 from the beginning of the fatigue phase provided low N_F. In specimen MB_300_60_B_F_1, a matrix crack occurred at the FDS loaded end and suddenly propagated along the textile plane, inducing a rapid increase of g/g_0 from 2 to 6. This crack, which was not present in other specimens, was attributed to poor adhesion between the two layers of matrix embedding the textile. The crack also affected k/k_0, and A_{cyc}. The slope suddenly decreased (Fig. 9b) and the area suddenly increased (Fig. 9c) as a results of the decrease in the bonded length available after the opening of the crack. k/k_0 decreased with increasing N for all specimens except for MB_300_60_B_F_2, where k/k_0 increased during the test. However, in all specimens A_{cyc} increased during the fatigue cycles, which indicated progressive damage at the matrix-fiber interface and of fiber filaments. The fatigue steady stage of specimens MB_300_60_B_F_1, 2, 3, and 4 ended at approximately 0.20, 0.47, 1.22, and 0.32×10^6 cycles. After this, g/g_0 rapidly increased and the specimen failed. The result scatter observed, which was attributed to the randomly distributed properties of the matrix-fiber interface, to the non-symmetrical behavior of the FRCM strips on the two prisms, and to possible misalignment between the two blocks, did not allow for identifying a clear effect of the fatigue cycles on the FRCM bond behavior. However, these results clearly showed the vulnerability of the fiber textile to cyclic loading, which induced progressive damage of fiber filaments leading to eventual rupture.

4.2. Bond-gap specimens

Fig. 9d shows the $g_e/g_{e,0} - N$ response for the tested specimens. All specimens showed a significant increase of the midspan displacement g_e at the beginning of the fatigue loading. As the number of cycles increased, specimens entered in a steady stage where $g_e/g_{e,0}$ increased almost linearly with the number of cycles. The steady stage lasted for 36, 16, 25, and 6×10^3 cycles for specimens MB_300_60_G_F_1, 2, 3 and 4. Similarly to bare-fiber specimens, the midspan displacement increase observed in the steady stage of bond-gap specimens could be attributed to a combined action of matrix-fiber debonding and progressive damage and rupture of fiber filaments. However, the limited extent of this stage in bond-gap specimens with respect to that in bare-fiber specimens suggested that fiber damage was higher for the former strip layout. This was also confirmed by a more rapid reduction in the 10-cycle blocks slope shown in Fig. 9e, whereas a similar behavior of the area A_{cyc} was observed for bare-fiber and bond-gap specimens (Fig. 9f). Eventually, with increasing the number of cycles specimens entered in a non-steady stage that lasted for approximately 25 % of their fatigue life. In this stage, a rapid increase in midspan displacement was observed until failure occurred due to rupture of the textile along the bond-gap length. LVDTs G3-G4 and G5-G6 (Fig. 3b) never recorded free-end slips of the textile, which indicated that debonding did not propagate until the strip free end and that the fatigue degradation and failure was mainly governed by fiber damaging and rupture.

Bond-gap specimens failed at a number of cycles N_F in the range 10×10^3 —42×10^3 (see Table 4). The fatigue life of bond-gap specimens resulted on average 94.5 % lower than that of nominally equal specimens with bare-fiber layout (Table 4). This indicated that, although the

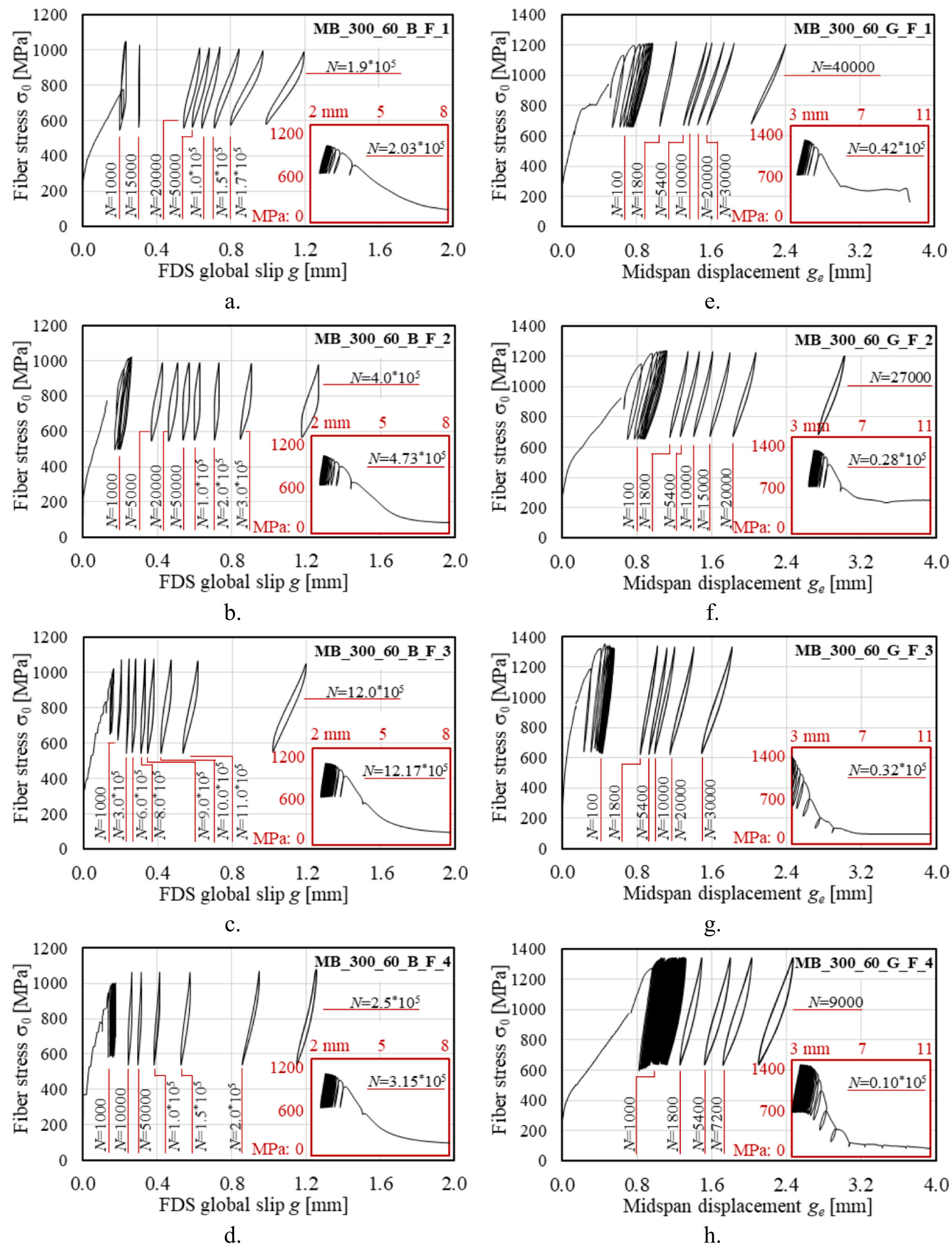

Fig. 8. Stress – global slip curve of specimen MB_300_60_B_F_ a) 1, b) 2, c) 3, and d) 4. Stress – midspan displacement curve of specimen MB_300_60_G_F_ e) 1, f) 2, g) 3, and h) 4.

presence of matrix at midspan increased the specimen quasi-static load-carrying capacity with respect to that of bare-fiber specimens (see Table 3), it increased the fiber damage during the fatigue loading leading to a substantially lower fatigue life with respect to that of bare-fiber specimens.

4.3. Post-fatigue behavior

Specimens tested under fatigue loading showed a progressive reduction of the cycle slope and an increase in cycle area. To clarify if the progressive matrix-fiber debonding or damage and rupture of fiber filaments was mainly responsible for the progressive degradation of the specimen mechanical properties during the fatigue steady stage, the fatigue test of MB with bond-gap layout MB_300_60_G_PF_1 and_2 were interrupted to perform a post-fatigue quasi-static monotonic test and assess the specimen post-fatigue capacity. The test consisted of three phases: (i) a displacement-controlled quasi-static monotonic test until the mean fatigue load was attained, (ii) a 10-thousand cycle fatigue loading stage (i.e., 33 % of the average fatigue life of bond-gap specimens, see Table 4), and (iii) a post-fatigue displacement-controlled quasi-static monotonic test until failure of the specimen.

Fig. 10 shows the fiber stress σ_0 – midspan displacement g_e curves of post-fatigue specimens. All specimens failed in the post-fatigue phase due to debonding at the matrix-fiber interface. The σ_0 – g_e responses showed an initial non-linear quasi-static monotonic branch, followed by 10-cycle blocks extracted every 2000 cycles during the fatigue-load phase. For both specimens MB_300_60_G_PF_1 and 2 (see Fig. 10a and b), an increase of the midspan displacement was recorded during the

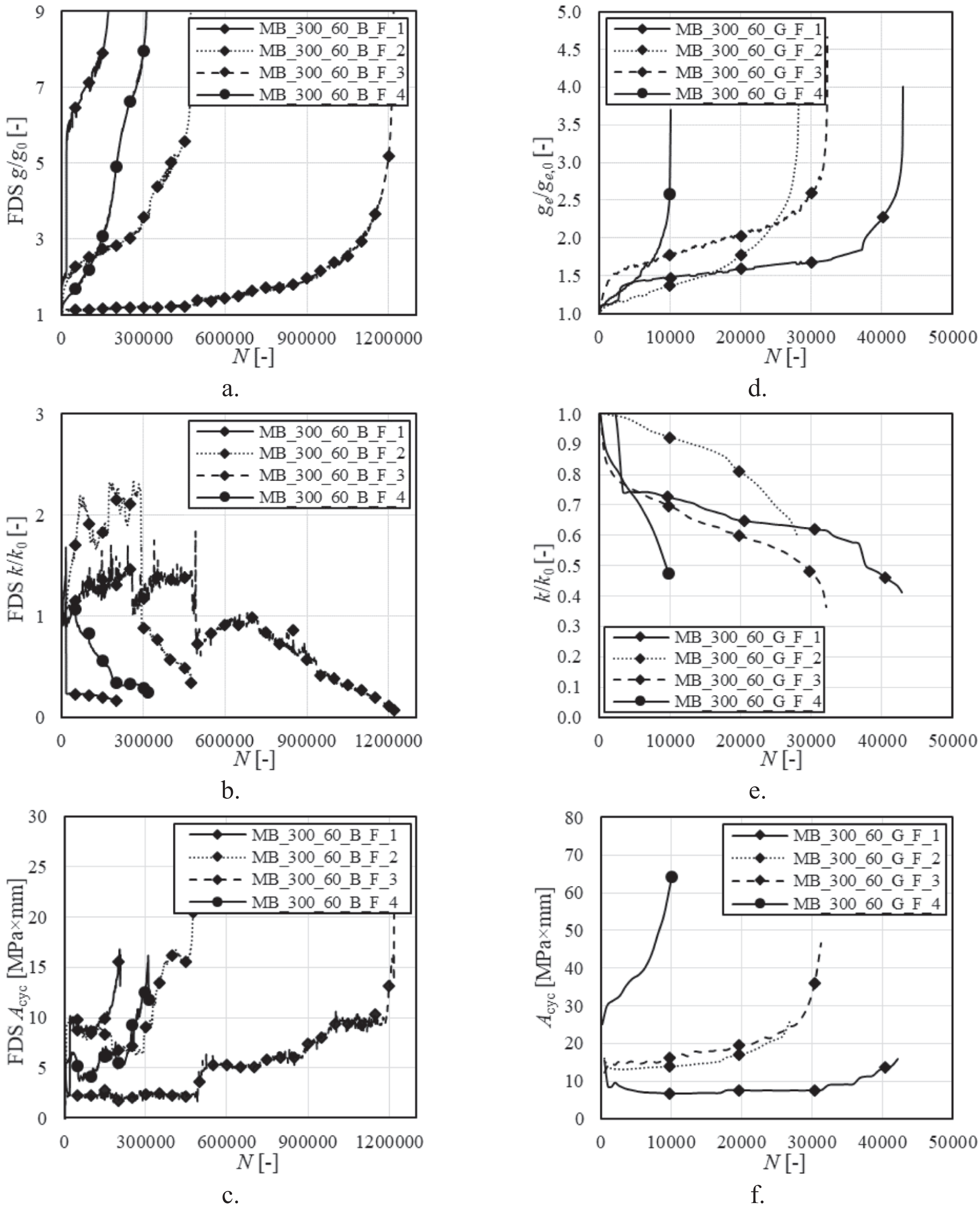

Fig. 9. Results of fatigue tests on MB specimens: variation of a) normalized global slip, b) normalized cycle secant slope, and c) cycle area with the number of cycles at the fully debonded side (FDS) of bare-fiber specimens. Variation of d) normalized midspan displacement, e) normalized cycle secant slope, and f) cycle area with the number of cycles for bond-gap specimens.

cyclic phase, which was associated with a progressive reduction of the cycle slope k and an increase of the area A_{cyc} (see Fig. 10c and d). In the post-fatigue phase, which started at the mean fatigue load, the response was initially linear with a slope similar to that of the last cycles. With increasing the machine stroke, the response became non-linear until the attainment of the peak stress $\sigma_0{}^*_{PF}$, which was associated with the midspan displacement $g_e{}^*_{PF}$. Eventually, the $\sigma_0 - g_e$ curve plateaued at a constant residual friction stress $\sigma_{0,f,PF}$.

Table 5 provides the main results obtained from specimens MB_300_60_G_PF, where N_{PF} is the number of load cycles of phase (ii). Specimens MB_300_60_G_PF_1 and 2 (see Fig. 10a and b) showed a post-fatigue peak stress $\sigma_0{}^*_{PF}$ 44 % and 41 % lower than the corresponding average quasi-static peak stress $\overline{\sigma}_0^* = 2543$ MPa (see Table 4), respectively. This significant reduction in the post-fatigue peak stress could be attributed to rupture of some fiber filaments occurred during the cyclic phase. Similarly, the post-fatigue residual friction stress $\sigma_{0,f,PF}$ resulted 57 % and 44 % lower than the corresponding average quasi-static residual friction stress $\overline{\sigma}_{0f} = 463$ MPa (see Table 4) for specimens MB_300_60_G_PF_1 and 2, respectively. This result could again be attributed to rupture of fiber filaments, which in turn determined a reduction of contact surface between fiber filaments and between matrix and fibers where the residual friction stress developed.

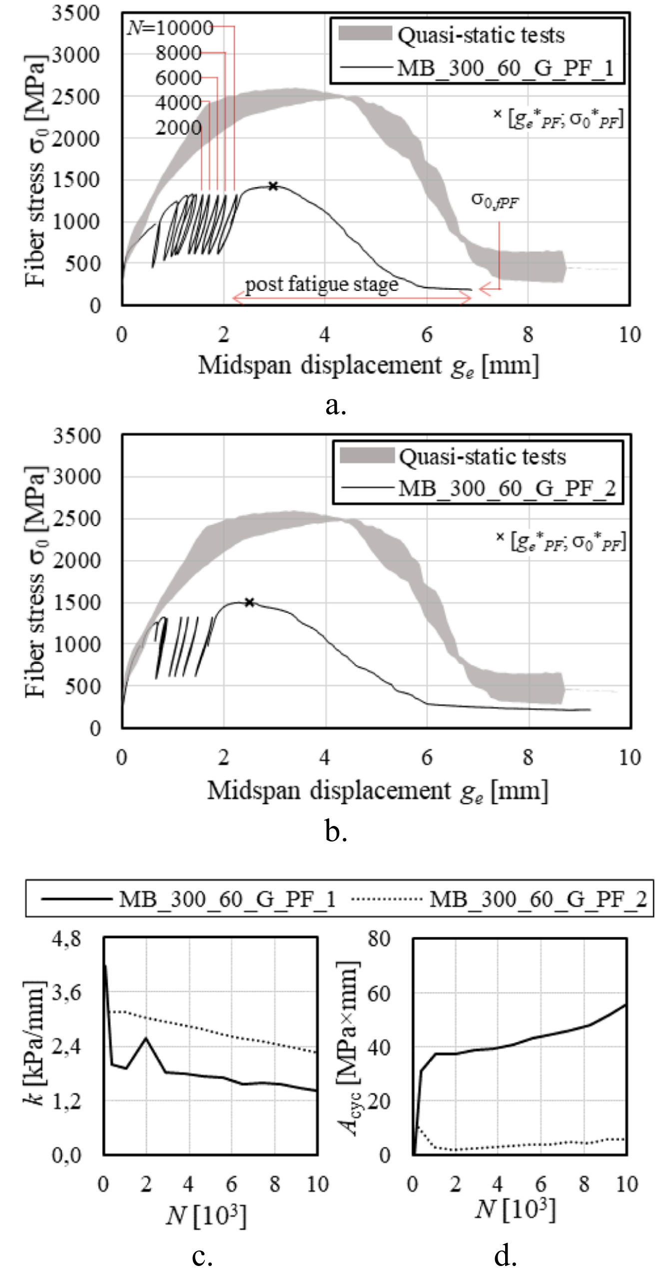

Fig. 10. Load responses of specimen a) MB_300_60_G_PF_1 and b) MB_300_60_G_PF_2. Variation of cycle slope and cycle area for specimen c) MB_300_60_G_PF_1 and d) MB_300_60_G_PF_2.

The results obtained showed that direct shear and bending tests with different composite layouts provide fundamental information on the composite bond behavior. The use of modified beams allowed for observing the detrimental effect of the cyclic load on the specimen capacity, which was less pronounced in corresponding fatigue direct shear tests. This confirms the importance of the study of matrix-fiber bond behavior and suggests the need of investigating the fatigue response of full-scale FRCM strengthened member to obtain results that closely reproduce the real application.

5. Conclusions

In this study, the use of FRCM composites to improve the fatigue behavior of RC members was investigated. First, a discussion on the responses of FRCM-strengthened beams subjected to fatigue loading was provided. Then, the results of an experimental campaign to study the fatigue and post-fatigue response of direct shear and modified beam test specimens comprising PBO FRCM composites and concrete prisms were provided and discussed. Based on the literature review and results herein presented, the following conclusions can be drawn:

- The reduction of tensile stress acting on the steel rebars of an existing RC beam attributed to the presence of the FRCM strengthening varied between 3.8 and 13.7 % for the specimens considered and appeared a linear function of the product between the composite cracked elastic modulus and cross-sectional area. However, it should be noted that in real applications these stress reductions may be lower because the FRCM strengthening is usually applied when part of the service load is already acting on the structure.
- Independently from the FRCM type employed and composite reinforcement ratio of specimens collated from the literature, the majority of the specimens with tensile rebars in the elastic range exhibited a composite exploitation ratio at cycle peak between 6.3 % and 18.8 %. Generally, a decrease of the FRCM exploitation was associated with an increase of specimen fatigue life. Exploitation ratios higher than 20 % at cycle peak were associated with yielded tension steel rebars.
- The modified beam test specimens subjected to fatigue loading failed due to rupture of the fiber filaments with a number of cycles at failure between 0.20×10^6 cycles and 1.22×10^6 cycles for bare-fiber layout specimens and between 0.10×10^5 cycles and 0.42×10^5 cycles for specimens with bond-gap layout. The failure mode did not allow for verifying whether the progressive matrix-fiber debonding or damage of the fiber was mainly responsible for the progressive degradation of the specimen stiffness.
- Fatigue test on bond-gap layout specimens showed a fatigue life 94.5 % lower than that of bare-fiber specimens. This difference was attributed to a more pronounced damage and rupture of fiber filaments caused by the embedding matrix (not bonded to the substrate) along the bond-gap length.
- Post-fatigue quasi-static tests of bond-gap layout specimens showed a lower bond and residual capacities than that of corresponding quasi-static tests. This can be attributed to rupture of fiber filaments during the cyclic stage.

The results obtained are valid only for the PBO FRCM composite studied. The failure mode observed, i.e., debonding at the matrix-fiber interface, showed the importance of the matrix-fiber bond properties and indicated that proper experimental testing is needed to investigate the behavior of FRCM comprising different matrix and fibers. Besides, the high scatter in the results of cyclic bond tests highlights the need for further research to fully assess the fatigue behavior of FRCM composites. The literature review, as well as results of FRCM-concrete specimen tests, showed the potential contribution of the EB composite to the strengthened member fatigue life. However, the stress applied to the

Table 5
Results of post-fatigue MB specimens with bond-gap layout.

Specimen	$\sigma_{0,\min}$ [MPa]	$\sigma_{0,\max}$ [MPa]	R_W [-]	N_{PF} [10^3]	$\sigma_0{}^*_{PF}$ [MPa]	$g_e{}^*_{PF}$ [mm]	$\sigma_{0,f,PF}$ [MPa]
MB_300_60_G_PF_1	611	1326	0.46	10	1425	2.98	205
MB_300_60_G_PF_2	616	1325	0.46	10	1499	2.50	258

composite and the presence of stresses normal to the interface where debonding occurs play a fundamental role and should be carefully controlled when designing the strengthening under cyclic load.

CRediT authorship contribution statement

Angelo Savio Calabrese: Formal analysis, Conceptualization, Investigation, Writing – original draft. **Pierluigi Colombi:** Conceptualization, Supervision, Validation, Writing – review & editing. **Tommaso D'Antino:** Conceptualization, Resources, Supervision, Validation, Writing – review & editing.

Declaration of competing interest

The authors declare that they have no known competing financial interests or personal relationships that could have appeared to influence the work reported in this paper.

Data availability

Data will be made available on request.

Acknowledgements

The financial support of the Politecnico di Milano, Italy is gratefully acknowledged by the authors.

References

[1] Pais JC, Amorim SIR, Minhoto MJC. Impact of traffic overload on road pavement performance. J Transp Eng 2013;139:873–9. https://doi.org/10.1061/(ASCE)TE.1943-5436.0000571.
[2] Rys D, Judycki J, Jaskula P. Analysis of effect of overloaded vehicles on fatigue life of flexible pavements based on weigh in motion (WIM) data. Int J Pavement Eng 2016;17:716–26. https://doi.org/10.1080/10298436.2015.1019493.
[3] Yi W, Kunnath S, Sun X, Shi C, Tang F. Fatigue behavior of reinforced concrete beams with corroded steel reinforcement. ACI Struct J 2010;107.
[4] Hobbacher AF. Recommendations for Fatigue Design of Welded Joints and Components. Cham: Springer International Publishing; 2016. https://doi.org/10.1007/978-3-319-23757-2.
[5] American Concrete Institute. 215R-92. Considerations for Design of Concrete Structures Subjected to Fatigue Loading 1997.
[6] European Committee for Standardization. Eurocode 2: Design of concrete structures - Part 1-1: General rules and rules for buildings. Brussels, Belgium: CEN; 2004.
[7] Herbrand M, Adam V, Classen M, Kueres D, Hegger J. Strengthening of existing bridge structures for shear and bending with carbon textile-reinforced mortar. Materials 2017;10:1099. https://doi.org/10.3390/ma10091099.
[8] Carloni C, Subramaniam K, Savoia M, Mazzotti C. Experimental determination of FRP–concrete cohesive interface properties under fatigue loading. Compos Struct 2012;94:1288–96. https://doi.org/10.1016/j.compstruct.2011.10.026.
[9] Ekenel M, Myers JJ. Fatigue performance of CFRP strengthened RC beams under environmental conditioning and sustained load. J Compos Constr 2009;13:93–102. https://doi.org/10.1061/(ASCE)1090-0268(2009)13:2(93).
[10] Gheorghiu C, Labossière P, Proulx J. Response of CFRP-strengthened beams under fatigue with different load amplitudes. Constr Build Mater 2007;21:756–63. https://doi.org/10.1016/j.conbuildmat.2006.06.019.
[11] Barnes RA, Mays GC. Fatigue performance of concrete beams strengthened with CFRP plates. J Compos Constr 1999;3:63–72. https://doi.org/10.1061/(ASCE)1090-0268(1999)3:2(63).
[12] American Concrete Institute. Guide to Design and Construction of Externally Bonded Fabric-Reinforced Cementitious Matrix (FRCM) and Steel-Reinforced Grout (SRG) Systems for Repair and Strengthening Masonry Structures. ACI 549.6R-20. Farmington Hills, 48331 MI: ACI; 2020.
[13] Donnini J, Spagnuolo S, Corinaldesi V. A comparison between the use of FRP, FRCM and HPM for concrete confinement. Compos Part B 2019;160:586–94. https://doi.org/10.1016/j.compositesb.2018.12.111.
[14] Calabrese AS, D'Antino T, Colombi P, Poggi C. Long-term behavior of PBO FRCM and comparison with other inorganic-matrix composites. Materials 2022;15. https://doi.org/10.3390/ma15093281.
[15] Al-Lami K, Calabrese AS, Colombi P, D'Antino T. Effect of wet-dry cycles on the bond behavior of fiber-reinforced inorganic-matrix systems bonded to masonry substrates. Materials 2021;14. https://doi.org/10.3390/ma14206171.
[16] Papanicolaou CG, Triantafillou TC, Papathanasiou M, Karlos K. Textile reinforced mortar (TRM) versus FRP as strengthening material of URM walls: out-of-plane cyclic loading. Mater Struct 2008;41:143–57. https://doi.org/10.1617/s11527-007-9226-0.
[17] Younis A, Ebead U, Shrestha KC. Different FRCM systems for shear-strengthening of reinforced concrete beams. Constr Build Mater 2017;153:514–26. https://doi.org/10.1016/j.conbuildmat.2017.07.132.
[18] Almeida JAPP, Pereira EB, Barros JAO. Assessment of overlay masonry strengthening system under in-plane monotonic and cyclic loading using the diagonal tensile test. Constr Build Mater 2015;94:851–65. https://doi.org/10.1016/j.conbuildmat.2015.07.040.
[19] Valluzzi MR, da Porto F, Garbin E, Panizza M. Out-of-plane behaviour of infill masonry panels strengthened with composite materials. Mater Struct 2014;47:2131–45. https://doi.org/10.1617/s11527-014-0384-6.
[20] Calabrese AS, D'Antino T, Colombi P. Experimental and analytical investigation of PBO FRCM-concrete bond behavior using direct and indirect shear test set-ups. Compos Struct 2021;267. https://doi.org/10.1016/j.compstruct.2021.113672.
[21] Donnini J, Corinaldesi V. Mechanical characterization of different FRCM systems for structural reinforcement. Constr Build Mater 2017;145:565–75. https://doi.org/10.1016/j.conbuildmat.2017.04.051.
[22] Santandrea M, Focacci F, Mazzotti C, Ubertini F, Carloni C. Determination of the interfacial cohesive material law for SRG composites bonded to a masonry substrate. Eng Fail Analys 2020;111:104322. https://doi.org/10.1016/j.engfailanal.2019.104322.
[23] Calabrese AS, D'Antino T, Colombi P, Poggi C. Low- and high-cycle fatigue behavior of FRCM composites. Materials 2021;14:5412. https://doi.org/10.3390/ma14185412.
[24] D'Antino T, Carloni C, Sneed LH, Pellegrino C. Fatigue and post-fatigue behavior of PBO FRCM-concrete joints. Int J Fatigue 2015;81:91–104. https://doi.org/10.1016/j.ijfatigue.2015.06.008.
[25] Calabrese AS, D'Antino T, Colombi P, Poggi C, Carloni C. Influence of the test set-up on the bond behavior of FRCM composites. ACI SP 2021;345:185–95.
[26] Ceroni F, Bonati A, Galimberti V, Occhiuzzi A. Effects of environmental conditioning on the bond behavior of FRP and FRCM systems applied to concrete elements. J Eng Mech 2018;144:04017144. https://doi.org/10.1061/(ASCE)EM.1943-7889.0001375.
[27] Alecci V, Focacci F, Rovero L, Stipo G, De Stefano M. Extrados strengthening of brick masonry arches with PBO–FRCM composites: experimental and analytical investigations. Compos Struct 2016;149:184–96. https://doi.org/10.1016/j.compstruct.2016.04.030.
[28] Elghazy M, El Refai A, Ebead U, Nanni A. Fatigue and monotonic behaviors of corrosion-damaged reinforced concrete beams strengthened with FRCM composites. J Compos Constr 2018;22:04018040. https://doi.org/10.1061/(ASCE)CC.1943-5614.0000875.
[29] Jie S, Shi-ping Y, Fei W, YangYang. Experimental study on the fatigue behaviour of RC beams strengthened with TRC after sustained load corrosion. Constr Build Mater 2017;131:713–20. https://doi.org/10.1016/j.conbuildmat.2016.11.030.
[30] Pino V, Akbari Hadad H, De. Caso y Basalo F, Nanni A, Ali Ebead U, El Refai A. Performance of FRCM-Strengthened RC Beams Subject to Fatigue. J Bridge Eng 2017;22:04017079. https://doi.org/10.1061/(ASCE)BE.1943-5592.0001107.
[31] Su MN, Wei LL, Liang HS, Zhu JH, Ueda T, Xing F. Fatigue behaviour and design of corroded reinforced concrete beams intervened by ICCP-SS. Compos Struct 2020. https://doi.org/10.1016/j.compstruct.2020.113295.
[32] Leung CKY, Cheung YN, Zhang J. Fatigue enhancement of concrete beam with ECC layer. Cem Concr Res 2007;37:743–50. https://doi.org/10.1016/j.cemconres.2007.01.015.
[33] Akbari Hadad H, Nanni A. Fatigue behavior of FRCM-strengthened RC beams. J Compos Constr 2020;24. https://doi.org/10.1061/(ASCE)CC.1943-5614.0001084.
[34] Calabrese AS, D'Antino T, Colombi P, Carloni C, Poggi C. Fatigue Behavior of FRCM Strengthened RC Beams: State of the Art and Future Developments. In: Ilki A, Ispir M, Inci P, editors. 10th International Conference on FRP Composites in Civil Engineering, Cham: Springer International Publishing; 2022, p. 201–12. Doi: 10.1007/978-3-030-88166-5_16.
[35] D'Antino T, Poggi C. Characterization and design of multilayer PBO FRCM composite reinforcements for concrete structures. J Compos Constr 2021;25:1–13. https://doi.org/10.1061/(ASCE)CC.1943-5614.0001155.
[36] Akbari Hadad H, Nanni A, Ebead UA, El Refai A. Static and fatigue performance of FRCM-strengthened concrete beams. J Compos Constr 2018;22:04018033. https://doi.org/10.1061/(ASCE)CC.1943-5614.0000868.
[37] Aljazaeri ZR, Myers JJ. Fatigue and flexural behavior of reinforced-concrete beams strengthened with fiber-reinforced cementitious matrix. J Compos Constr 2017;21:04016075. https://doi.org/10.1061/(ASCE)CC.1943-5614.0000726.
[38] Arboleda D, Carozzi FG, Nanni A, Poggi C. Testing procedures for the uniaxial tensile characterization of fabric-reinforced cementitious matrix composites. J Compos Constr 2016;20:04015063. https://doi.org/10.1061/(ASCE)CC.1943-5614.0000626.
[39] Jabr A, El-Ragaby A, Ghrib F. Effect of the Fiber Type and Axial Stiffness of FRCM on the Flexural Strengthening of RC Beams. Fibers 2017;5:2. https://doi.org/10.3390/fib5010002.
[40] Signorini C, Nobili A, Sola A, Messori M. Designing epoxy viscosity for optimal mechanical performance of coated glass textile reinforced mortar (GTRM) composites. Constr Build Mater 2020;233:117325. https://doi.org/10.1016/j.conbuildmat.2019.117325.
[41] D'Antino T, Focacci F, Carloni C, Sneed LH. Relationship between the effective strain of FRCM-strengthened RC beams and the debonding strain of direct shear tests. Eng Struct 2020;216:1–16. https://doi.org/10.1016/j.engstruct.2020.110631.
[42] International Code Council Evaluation Service (ICC-ES). Acceptance criteria for masonry and concrete strengthening using fabric-reinforced cementitious matrix

(FRCM) and steel reinforced grout (SRG) composite systems. AC434. Whittier, CA: 2018.
[43] National Research Council. Guide for the design and construction of externally bonded fibre reinforced inorganic matrix systems for strengthening existing structures. CNR-DT 215/2018. Rome, Italy: CNR; 2018.
[44] Calabrese AS, D'Antino T, Colombi P, Carloni C, Poggi C. Fatigue behavior of PBO FRCM composite applied to concrete substrate. Materials (Basel) 2020;13. https://doi.org/10.3390/ma13102368.
[45] Ente Nazionale Italiano di Unificazione. UNI EN 12390-3:2019. Testing hardened concrete - Part 3: Compressive strength of test specimens 2019.
[46] Ruregold srl. Technical datasheet of PBO-Mesh Gold 70/18 2019.
[47] Ruregold srl. Technical datasheet of MX-PBO calcestruzzo 2020.
[48] EOTA. EAD 340275-00-0104: Externally-bonded composite systems with inorganic matrix for strengthening of concrete and masonry structures 2018.
[49] Bertolli V, D'Antino T. Modeling the behavior of externally bonded reinforcement using a rigid-trilinear cohesive material law. Int J Solids Struct 2022;248:111641. https://doi.org/10.1016/j.ijsolstr.2022.111641.
[50] UNI EN 1015-11, Metodi di prova per malte per opere murarie – Determinazione della resistenza a flessione e a compressione della malta indurita n.d.
[51] Focacci F, D'Antino T, Carloni C. The role of the fiber–matrix interfacial properties on the tensile behavior of FRCM coupons. Constr Build Mater 2020;265:1–13. https://doi.org/10.1016/j.conbuildmat.2020.120263.
[52] Bilotta A, Lignola GP. Effects of defects on bond behavior of fiber reinforced cementitious matrix materials. Materials 2020;13. https://doi.org/10.3390/ma13010164.